Alumina toughened zirconia reinforced with equiaxed and elongated lanthanum hexa-aluminate precipitates

Maoyin Li[1], Bart Van Meerbeek[2], Bensu Tunca[1], Stevan Cokic[2], Jef Vleugels[1], Fei Zhang[2,1*]

[1] KU Leuven (University of Leuven), Department of Materials Engineering, Kasteelpark Arenberg 44, B-3001 Leuven, Belgium.

[2] KU Leuven (University of Leuven), Department of Oral Health Sciences, BIOMAT - Biomaterials Research group & UZ Leuven (University Hospitals Leuven), Dentistry, Kapucijnenvoer 7 block a, B-3000 Leuven, Belgium.

Abstract

Three different alumina sources (boehmite, aluminium nitrate and α-alumina particles) and 12Ce-TZP powder containing 1 wt% lanthanum oxide were used to prepare 12Ce-TZP-based alumina-toughened-zirconia (ATZ) composites. The obtained ATZs had similar density and phase composition, whereas the microstructures were significantly different. Alumina-particle addition gave rise to a typical ATZ microstructure consisting of equiaxial sub-micrometer zirconia and alumina phases, while the lanthanum hexa-aluminate phase was formed in large and non-homogenously distributed precipitates (~3.5 μm in length). The boehmite and aluminium nitrate-based composites contained not only sub-micrometer equiaxial alumina and zirconia grains but also small-sized lanthanum hexa-aluminate precipitates (~1.2 μm in length) that were inter- and transgranularly positioned in the zirconia matrix and effectively promoted crack deflection and toughening. In combination with a higher *t*-ZrO_2 transformability, the boehmite-based composites had a higher indentation fracture resistance, strength and reliability compared to the aluminium-nitrate and alumina-particle based equivalents.

Key words: Microstructure; Alumina-toughened-zirconia; Alumina precursors, Elongated lanthanum hexa-aluminate precipitates

1. Introduction

In pursuit of tougher, stronger and more reliable ceramics, zirconia remains one of the most promising ceramics [1]. In order to benefit from transformation toughening, tetragonal zirconia needs to be maintained at room temperature by alloying pure zirconia with stabilizing oxides such as Y_2O_3, CeO_2, CaO or MgO [2]. Among the different zirconia ceramics, yttria-stabilized tetragonal zirconia polycrystalline (Y-TZP) ceramics, usually containing 3 mol% yttria, have a wide application range, such as bearings, fuel cell supports, wear parts, knives, and most recently dental restorations and biomedical implants due to their fine microstructure and high strength [3–5]. However, due to a limited transformation toughening zone width, 3Y-TZP ceramics in general have a moderate fracture toughness, ranging from 3 to 5 MPa $m^{1/2}$ [6]. Some Y-TZP ceramics also suffer from low temperature degradation (LTD) or hydrothermal aging when used in the presence of water. This could be critical for dental applications because of the exposure to various factors in the oral cavity such as aqueous saliva, pH and temperature changes, and cyclic loading during chewing that could increase the risk of LTD [7,8]. Alternatively, zirconia-based ceramics such as ceria-stabilized tetragonal zirconia (Ce-TZP) and alumina-toughened Ce-TZP zirconia composites (ATZ) are of high interest since Ce-TZP has a superior fracture toughness (6-16 MPa $m^{1/2}$) [9] in addition to a high resistance to hydrothermal aging [11,12]. The coarser microstructure of Ce-TZP however limits the mechanical properties, especially the flexural strength as compared to Y-TZP [2,12,13]. Alumina addition as secondary phase, like in ATZ, can effectively suppress the grain coarsening kinetics of the Ce-TZP matrix during sintering by grain boundary pinning [14,15].

Besides, alumina bonds are less prone to chemisorption of polar water molecules and are less sensitive to water assisted stress corrosion or slow crack growth [16–18]. Therefore, alumina-toughened-zirconia with a Ce-TZP matrix is promising to manufacture long-term reliable and stable biomaterials especially for dental applications such as implants and abutments.

A decreased zirconia-grain size by secondary alumina-particle addition contributes to a better flexural strength and aging resistance but at the expense of fracture toughness [19,20]. The grain size control of *t*-ZrO_2 becomes meaningful in balancing fracture toughness and strength and has been reported to be modifiable by sintering temperature or alumina content [21–24]. On the other hand, introducing proper elongated precipitates is an effective method to increase the fracture toughness in ATZ composites [12,14,25]. The elongated precipitate acts as an effective toughening agent by inducing large-angle crack-deflection/bridging mechanisms. These elongated precipitates also contribute to a fine *t*-ZrO_2 microstructure and higher fracture strength [19,26]. In order to introduce elongated precipitates, direct addition of synthesized elongated precipitates and *in-situ* generation are commonly used methods. Many reports on elongated precipitates in zirconia ceramics concern strontium hexa-aluminates, such as *in-situ* formed strontium hexa-aluminate ($SrAl_{12}O_{19}$ = SA_6) platelets in a 12Ce-TZP matrix [27], the Biolox Delta ATZ material from CeramTec, HTZ500 (2Y-TZP with 5 vol% dispersed $SrAl_{12}O_{19}$ particles) [28] and the Longlife ATZ grade developed by INSA Lyon and Politecnico di Torino (11Ce-TZP with 8 vol% Al_2O_3 and 8 vol% $SrAl_{12}O_{19}$ composite produced by the surface modification method) [14]. However, only very few reported studies were available on lanthanum hexa-aluminate containing zirconia based ceramics [29–33]. Furthermore, different forms of elongated precipitates can be generated by different processing methodologies even with the same overall composition [14,25,34]. *In-situ* formed large-sized strontium or lanthanum hexa-aluminate elongated precipitates were reported

to have a negative effect on both fracture toughness and strength of 12Ce-TZP based composites, as compared to alumina particle additions [25]. The dimensional control of elongated precipitates seems to be critical because large-sized elongated precipitates can also act as critical defects [25], while the particle size and chemical reactivity of alumina are reported to be the main factors governing the dimensions of elongated aluminate precipitates [35]. Usually, alumina is added in the form of Al_2O_3 particles or alumina precursors at a content allowing to tailor the zirconia-grain size, hereby modifying the mechanical properties and improving the low-temperature aging resistance.

However, very limited information is available on alumina precursors to control the formation of the secondary phase alumina in ATZ and a clarification of the different formation mechanisms of lanthanum hexa-aluminate precipitates is also missing. Therefore, in this work, the influence of using different alumina precursors on the microstructure, mechanical properties and hydrothermal aging behavior of 12Ce-TZP based ATZ ceramics was investigated and compared with α-Al_2O_3 powder-based ATZ.

2. Materials and methods

2.1. Materials

To generate homogeneously dispersed elongated lanthanum hexa-aluminate precipitates, commercially available 12Ce-TZP (CEZ12-1, Lot No. A0923, Daiichi Kigenso Kagaku Kogio, Japan) containing 1 wt% La_2O_3 was used as zirconia-starting powder. Boehmite (γ-AlOOH, Dispersal P2, Sasol, Germany) and aluminium nitrate ($Al(NO_3)_3 \cdot 9H_2O$, ≥98%, ChemPur, Germany) were used as alumina precursors for comparison with α-alumina particles (α-Al_2O_3, Lot No. 9235, BET specific surface area 14.5 m^2/g and a primary particle size of 0.1 μm, TM-DAR,

Taimicron, Taimi Chemical, Japan). The nominally 20 wt% Al_2O_3 containing sintered composites processed from boehmite, α-alumina particles and aluminium nitrate were referred to as 12-20B, 12-20P and 12-20N, respectively. The starting powders for 12-20B and 12-20P were mixed (Turbula type T2C, Basel, Switzerland) for 24 hours with 5 mm Y-TZP (grade TZ-3Y, Tosoh, Japan) milling balls in ethanol. The powders for 12-20N were mixed in the same way but in water. To avoid the influence of the thermal decomposition of aluminium nitrate on the ceramic density, ammonium hydroxide (extra pure, 25% solution in water, Lot No. A0378959, Acros Organics, USA) was added to the suspension at room temperature to adjust the pH to 10 under continuous magnetic stirring. The ammonium nitrate and excess ammonium hydroxide in suspension were removed by washing with demineralized water and centrifugation at 8000 rpm for 2 min until the pH of the suspension was 7. All suspensions were dried in a rotary evaporator at 60°C, followed by drying in an oven at 90°C for 12 hours. The dried powders were sieved through a 315-μm mesh sieve. All powders were shaped by uniaxial pressing of 20-mm diameter discs at 225 MPa for 40 seconds (Nannetti Mignon SSN/EA, Nannetti, Italy), followed by cold isostatic pressing (CIP, EPSI, Temse, Belgium) at 300 MPa for 1 min. Pressureless sintering was performed in air in a conventional furnace (Nabertherm, Germany) for 2 hours at 1500°C with a heating and cooling rate of 5°C/min.

2.2. Material characterization

All processed ceramics were characterized with respect to phase composition, density, microstructure, Vickers hardness, indentation fracture resistance, biaxial bending strength and hydrothermal stability.

Phase identification was done by X-ray diffraction (XRD, 3003-T/T, Seifert, Ahrensburg, Germany) on polished specimens using Cu-K_α radiation (40 kV and 40 mA) from 20 to 90° 2θ with a step size of 0.02° for 2 s. The amount of monoclinic ZrO_2-phase was calculated according to the equation proposed by Garvie *et al* [36] and modified by Toraya *et al* [37].

$$V_m = \frac{1.311[I_m(\bar{1}11) + I_m(111)]}{1.311[I_m(\bar{1}11) + I_m(111)] + I_t(101)} \quad (1)$$

The peak intensity for the monoclinic (-111 and 111) and tetragonal (101) phases are represented by the subscripts *m* and *t*. The lattice parameters and cubic phase content were quantified by Rietveld refinement using Topas academic software (Bruker AXS, Karlsruhe, Germany), with the tetragonality of the *t*-ZrO_2 phase having been defined as $c/(\sqrt{2}a)$. The phase structures were refined as: tetragonal zirconia (t) unit cell with space group $P42/nmc$, monoclinic zirconia (m) unit cell with space group $P21/c$, and cubic zirconia (c) with space group $Fm\bar{3}m$. To calculate the *t*-ZrO_2 phase transformability, the *t*-to-*m* phase transformation on polished and fracture surfaces were assessed using XRD in the 27 to 33° 2θ range.

The density was measured in ethanol according to the Archimedes principle and referred to the theoretical density (TD) that was calculated by the rule of mixtures. The density of *c*, *t* and *m*-ZrO_2 was calculated by the ratio of molecular weight to the volume of unit cell, whereas the densities of alumina and lanthanum hexa-aluminate were taken as 3.99 $g \cdot cm^{-3}$ and 4.17 $g \cdot cm^{-3}$ [38]. Scanning electron microscopy (SEM; FEI-Nova Nanosem 450, FEI, Eindhoven, The Netherlands) was used to characterize the microstructure on mirror-polished, thermally etched (1300°C for 25 min in air) and Pt-coated cross-sections. The grain size of the zirconia, alumina and lanthanum hexa-aluminate phases was quantified according to the linear intercept method using IMAGE-PRO software (Media Cybernetics, Silver Spring, USA). The mean size and standard deviation are

reported without any correction. Samples for transmission electron microscopy (TEM) were prepared by FIB (Nova NanoLab 600 DualBeam, FEI), using a Pt coating as protective layer, 30 kV Ga ions for milling and 2 kV Ga ions for cleaning. During TEM examinations (Jeol ARM200F, operated at 200 kV), selected area electron diffraction (SAED) patterns were collected for phase identification, in combination with energy dispersive X-ray spectroscopy (EDS) elemental mapping in the scanning transmission electron microscopy (STEM) mode. STEM imaging was done using a high-angle annular dark field (HAADF) detector.

The Vickers hardness (GPa) and indentation fracture (IF) resistance ($MPa{\cdot}m^{1/2}$) were measured on an indentation tester (Model FV-700, Future-Tech, Tokyo, Japan) with a load of 98.1 N for 10 s. Ten measurements were performed on each sample. The fracture toughness was calculated from the radial crack pattern of Vickers indentations according to the Niihara *et al*. equation for Palmqvist cracks [39]. The E-modulus of the three ceramics was calculated by the rule of mixtures, as given in equation (2) [40,41].

$$E = (E_{12CE-TZP} \times V_{12CE-TZP}) + (E_{\alpha-Al2O3} \times V_{\alpha-Al2O3}) \quad (2)$$

with $E_{12Ce-TZP}$ (194 GPa) [42], $E_{Al_2O_3}$ (395 GPa) [43], $V_{12Ce-TZP}$ and $V_{Al_2O_3}$ being the Young's modulus and volume fraction for the 12Ce-TZP and α-Al_2O_3 phases, respectively. The indentation-induced cracks were investigated by SEM to analyze the crack propagation modes.

The hydrothermal stability was assessed by autoclaving mirror-polished specimens in steam at 134°C and 0.2 MPa for 150 hours, upon which the surface-phase transformation was assessed by XRD. The biaxial flexure strength was measured on discs (18 specimens per group) with a piston-on-three-balls testing fixture with a 1.6-mm diameter of the piston using a servo-hydraulic testing machine (Instron 4467, Norwood, MA, USA). Plane-parallel discs were loaded to failure at a

crosshead speed of 0.5 mm/min. Samples were prepared according to ISO 6872 [44] but the tensile surface was mirror-polished, whereas the opposite side was polished with a 15-μm diamond suspension. The biaxial fracture strength was calculated as [44]:

$$\sigma = -\frac{0.2387P(X-Y)}{b^2} \quad (3)$$

where σ is the maximum center tensile stress (MPa) and P the total load (N) causing fracture;

$$X = (1+\upsilon)\ln(r_2/r_3)^2 + [(1-\upsilon)/2](r_2/r_3)^2 \quad (4)$$

$$Y = (1+\upsilon)\left[1+\ln\left(\frac{r_1}{r_3}\right)^2\right] + (1-\upsilon)\left(\frac{r_1}{r_3}\right)^2 \quad (5)$$

with υ being the Poisson ratio (0.3), r_1 the radius of the support circle (6 mm), r_2 the diameter of the loaded area (0.8 mm), r_3 the specimen radius (in the range of 7.75 ± 0.2 mm) and b the specimen thickness at the fracture origin (1.2 ± 0.1 mm). The bending strength results were analyzed by Weibull statistics to assess the reliability of the sintered ceramics. The Weibull characteristic strength (σ_0) is the strength value at a probability of failure of 63.2%.

3. Results and discussion

3.1. Phase composition

The XRD patterns of the polished surfaces are presented in Fig. 1. *t*-ZrO_2 and α-Al_2O_3 phase peaks could be identified in the diffraction patterns, whereas the peaks of *c*-ZrO_2 (distinguishing peaks in between the doublet peaks of tetragonal phases) and *m*-ZrO_2 could not be clearly observed; Rietveld refinement confirmed the low content of cubic zirconia (~1.5 vol%). The peak for the elongated precipitate phase (see below), however, was too weak to quantify its content. The quantified phase composition and *t*-ZrO_2 tetragonality ($c/(\sqrt{2}a)$ of the three ceramic composites

by Rietveld refinement are presented in Table 1. The boehmite (12-20B) and aluminium nitrate (12-20N) based ceramics had a similar phase composition as compared to the α-alumina (12-20P) based composite. Due to the very limited amount of *m*-ZrO_2 and *c*-ZrO_2, the zirconia matrix in these composites can be considered as fully tetragonal zirconia. This is different than for the widely used 3Y-TZP ceramics, which normally contain about 20 vol% of cubic zirconia, despite the fact they are referred to as 3 mol% Yttria-doped Tetragonal Zirconia Polycrystal [45,46]. The Al_2O_3 content in all three sintered composites was about 28 vol%. The alumina-precursor type had no effect on the *t*-ZrO_2 lattice parameters, since the ZrO_2 matrixes showed the same level of lattice distortion (tetragonality).

3.2. Microstructure

All three alumina precursors resulted in near fully dense composites with a relatively density above 99.3%. Representative SEM micrographs of the three ceramics are comparatively shown in Fig. 2, revealing considerably different microstructures, in particular regarding the morphology of the elongated precipitates and the grain size of the zirconia and alumina phases. Besides the Al_2O_3 particles with dark atomic number contrast, high aspect ratio grains with a slightly brighter dark contrast, which were proven to be plate-like crystals, were observed in all studied composites [33]. Interestingly, these elongated precipitates in 12-20B and 12-20N were very fine grains (~1.2 μm in length with an aspect ratio of 5.6), occupying both inter- and intragranular positions in the zirconia matrix, whereas large-sized elongated precipitates (3.5 μm in length with an aspect ratio of 4.4) were formed in the alumina particle-based ATZ (12-20P). The large-sized platelets incorporated some zirconia grains, leading to incoherent grain boundaries in 12-20P.

The zirconia and alumina grain-size distributions and the length of the elongated lanthanum hexa-aluminate are presented in Fig. 3, with their average grain sizes being summarized in Table 2. The

α-alumina particle-based ATZ had the smallest alumina grain size (335 nm), followed by the aluminium-nitrate (453 nm) based ceramic. The boehmite-based ATZ had a substantially larger alumina grain size (759 nm). The larger secondary phase grain size implies a reduced Zener pinning effect on the movement of the zirconia-grain boundaries during sintering [47]. As a result of that, coarser zirconia grains were formed in 12-20B (1018 nm). Even though the alumina phase in 12-20P is smaller than that in 12-20N, which should have resulted in a finer zirconia matrix in 12-20P, the formation of smaller-sized elongated precipitates in 12-20N finally resulted in a smaller zirconia-grain size as compared to 12-20P.

TEM/STEM-EDS examinations (Fig. 4) were performed to assess the distribution of all involved elements and in particular to identify the observed elongated precipitates that were not detected by XRD due to their low content. Clearly, zirconium and cerium ions were only present in the zirconia grains (brighter grains). Aluminum ion was present in the darker equiaxial and elongated grains, which were proven by EDS to be alumina and lanthanum hexa-aluminate, respectively. The SAED patterns collected from these elongated grains were indexed as the lanthanum hexa-aluminate phase ($P6_3mc$) along the zone axes (Z.A.) of $[2\bar{1}\bar{1}0]$ and $[01\bar{1}0]$ [48]. Regarding the stoichiometry of the lanthanum hexa-aluminate phase, quantified areas from the STEM-EDS elemental maps showed that the indexed elongated phase contained 2.7 at% La, 35.2 at% Al, 60.1 at% O (1.2 at% Ce and 0.8 at% Zr). Although lanthanum hexa-aluminate phase is widely noted as $LaAl_{11}O_{18}$ [33,35,49,50], an ideal stoichiometric $LaAl_{11}O_{18}$ phase generally cannot be formed while non-stoichiometric compositions with an Al/La ratio in the range of 11-14 have been reported for hexa-aluminate structures [51–53]. Our result agrees with this expected ratio. Regarding the different sizes of the lanthanum hexa-aluminate phase in the different composites, as summarized in Table 2, using boehmite and aluminium nitrate as alumina precursors resulted in homogeneously

dispersed small-sized lanthanum hexa-aluminates ($La_{0.9}Al_{11.7}O_{20.0}$), whereas the alumina particles resulted in large-sized precipitates. This is because the alumina precursors during the phase transition effectively promoted the reaction between alumina and lanthanum oxide. In 12-20B, the γ-Boehmite transforms to α-Al_2O_3 via a sequence of alumina transitions (γ-Al_2O_3 → δ-Al_2O_3 → θ-Al_2O_3) during the sintering process [54,55]. In 12-20N, aluminium nitrate was transformed into aluminium hydroxide, i.e. bayerite (α-$Al(OH)_3$), in suspension at pH=10 [56], because aluminium nitrate as a direct alumina precursor would have resulted in a porous microstructure due to the decomposition of aluminium nitrate during sintering [57]. The bayerite loses physically adsorbed and crystalline water and transforms into γ-Al_2O_3 at around 300°C, and similarly as in 12-20B, this γ-Al_2O_3 transforms into α-Al_2O_3 via alumina mesophases at higher temperature [55,56]. In this case, the intermediate transformation stage from γ-Al_2O_3 to α-Al_2O_3 at 1200°C thermodynamically favors the formation of the hexagonal crystal structure, which enhanced the incorporation of La^{3+} ions to create a higher number of nuclei of lanthanum hexa-aluminate crystals leading to the formation of the small-sized lanthanum hexa-aluminate [33,58]. The reaction process for producing lanthanum hexa-aluminate by γ-Al_2O_3 is the same as for α-Al_2O_3 particles, but the reaction temperature was lowered about 100°C by using γ-Al_2O_3 particles forming a high density of lanthanum hexa-aluminate nuclei [33]. Therefore, the size of the lanthanum hexa-aluminate phase in boehmite and aluminium nitrate (aluminium hydroxide) based composites was effectively decreased and was homogeneously dispersed.

Finally, lanthanum ions, although originating from the merely 1 wt% La_2O_3 in the starting powder, were not only present in lanthanum hexa-aluminate but also in the zirconia grains. STEM/EDS showed that (1) La^{3+} was segregated at the grain boundaries of the zirconia grains in a space charge layer of about 2 nm thick (Fig. 5a), and (2) La^{3+} was also segregated at the lanthanum hexa-

aluminate-zirconia boundary (Fig. 5b), whereas lanthanum hexa-aluminate exhibited a higher and homogeneously distributed La^{3+} concentration than the Ce-stabilised ZrO_2 grains. This is different from the strontium hexa-aluminate $SrAl_{12}O_{19}$ - Ce-TZP system, in which strontium is only present inside the elongated $SrAl_{12}O_{19}$ precipitates [14]. The dissolution of Sr^{2+} with an ionic radius of 118 pm into the ZrO_2 host lattice is highly unfavorable due to a too large mismatch with Zr^{4+} (72 pm) [59] as compared to La^{3+} (103 pm). The presence of lanthanum ions in both zirconia and lanthanum hexa-aluminate grains can complicate the control of their compositional features, but the segregation of lanthanum ions in the space-charge layers at the zirconia-grain boundaries was reported to increase the aging-stability of zirconia grains [60]. Importantly, it was shown that 3Y-TZP ceramic with segreagted La^{3+} at the 2 nm space-charge layer of zirconia grains was able to maintain its crack resistance without overstabilitzing the zirconia grains [61], while in the present stuided system, segregated La^{3+} at the lanthanum hexa-aluminate-zirconia boundary may benefit the crack-deflection ability as well (see below).

3.3. Mechanical properties

The E-modulus of studied composite obtained by equation (2) is 253 GPa and the measured mechanical properties of 12-20P, 12-20B and 12-20N are summarized in Table 3.

Using α-alumina particles led to a slightly higher hardness (11.5 ± 0.1 GPa) than with boehmite (10.6 ± 0.1 GPa) or aluminium nitrate (11.1 ± 0.1 GPa), which is due to the finer microstructure of 12-20P. On the other hand, 12-20B had a higher indentation fracture resistance (9.7 ± 0.5 $MPa \cdot m^{1/2}$) than 12-20P (6.7 ± 0.3 $MPa \cdot m^{1/2}$) and 12-20N (8.0 ± 0.5 $MPa \cdot m^{1/2}$). This is in line with the higher *t*-ZrO_2 transformability in 12-20B thanks to the larger zirconia-grain size [62,63] as well as the stronger crack-deflection effect from the fine needle-shaped lanthanum hexa-aluminate phase.

As illustrated in Fig. 6, the differences in microstructure influenced the crack-propagation path, while the elongated $La_{0.9}Al_{11.7}O_{20.0}$ grains and coarser microstructure in 12-20B played an active role in promoting crack deflection. Cracks in 12-20B propagated along the interface between alumina and zirconia grains. A tortuous crack path was clearly observed (Fig. 6b), which could be attributed the segregation of lanthanum ions to grain-boundary. The grain-boundary segregation of La^{3+} may have resulted in the formation of a nanometric $La_{0.9}Al_{11.7}O_{20.0}$ foil around the alumina grains showing mechanically weak cleavage planes between the stacked spinel blocks [64,65]. This also explains the relatively weak grain boundary between the elongated $La_{0.9}Al_{11.7}O_{20.0}$ and zirconia grains, which induced an intergranular crack-propagation mode and a near 90° crack deflection, (Fig. 6c). At the crack-propagation tip (Fig. 6a), the main fracture is related to micro-cracking of the zirconia matrix, which is possibly caused by the zirconia transformation around the crack tip, thereby suppressing the main propagating crack, which can toughen a ceramic with R-curve behavior [66,67]. Some short crack branches were observed as well in 12-20B, as shown in Fig. 6c. In contrast, the fine alumina grains in 12-20P did not seem to significantly promote crack deflection (Fig. 6e-g). The elongated precipitates in 12-20P were much larger than in 12-20B and 12-20N, and are inferior in quantity. As a result, crack deflection by Al_2O_3-particle based $La_{0.9}Al_{11.7}O_{20.0}$ has not been reported. As shown in Fig. 6g, the interface between zirconia and elongated $La_{0.9}Al_{11.7}O_{20.0}$ grains was of an irregular/serrated nature, which might have given rise to more difficult intergranular cracking in 12-20P. A similar conclusion was drawn in other reports, where cracks propagated through this secondary reinforcement because of the strong bonding interface with zirconia [25]. In addition, even though the zirconia-grain size in 12-20N (662 ± 387 nm) is smaller than in 12-20P (705 ± 374 nm), which also resulted in a lower zirconia-phase transformability (16 vol%) in comparison with 12-20P (17 vol%), 12-20N had a higher indentation

fracture resistance. This can only be explained by the fine elongated $La_{0.9}Al_{11.7}O_{20.0}$ precipitates in 12-20N that contribute to the crack deflection efficiency, as in 12-20B.

It is noteworthy that the indentation fracture method employed in this work can only be considered to be semi-quantitative and was used to quickly compare the toughening effect between the same class of materials. It is however not the most reliable way to determine the true fracture toughness and it can be severely influenced by the R-curve and the slow crack growth phenomena [68]. In particular, the short cracks generated during indentation toughness measurement may not fully address the crack deflection toughening by the hex-aluminate platelets and in case of large transformation zone, i.e. the cases where cracks does not extend well out the of plastic deformation zone of the indent. Other methods such as single edge V-notch beam and double torsion will further be needed to determine a reliable fracture toughness.

The biaxial bending strength Weibull distribution is presented in Fig. 7. The composites had a comparable characteristic strength σ_0(12-20B) = 976 MPa, σ_0(12-20P) = 962 MPa and σ_0(12-20N) = 939 MPa, which was at least 400 MPa higher than reported for 12Ce-TZP (about 500 MPa) [10,29]. However, the 12-20B composite with higher indentation fracture resistance (9.7 ± 0.5 $MPa \cdot m^{1/2}$) also had a high Weibull modulus (m) of 20.7. This is substantially higher than for 12-20P (m=11.6) and 12-20N (m=14.1) and some reported ceria-TZP/alumina composite: 10Ce-TZP/alumina composite (m=12.6) [17], 10Ce-TZP/$MgAl_2O_4$ composite (m=10.1) [69] and 3Y-ATZ (m=8.24) [70]. The Weibull strength distribution reflects the critical flaw size distribution in the material [71], revealing the reliability of the material, and the Weibull modulus (i.e. scatter of the strength values) depends on various aspects including the process conditions, surface treatments [72] and methodologies of flexural tests with different effective stressed volume [73]. In the present work, under the identical aforementioned aspects, the fracture resistance or the crack

propagation resistance of the material significantly influenced the reliability of the studied composites, since it inevitably determines the critical flaw size and the defect tolerance window. It has also been reported that when having a significant amount of phase transformation-induced plasticity along with an effective transformation before failure, an excellent reliability (e.g. m=60) can be obtained [12,73]. Even though transformation-induced plasticity was not clearly detected for 12-20B during the biaxial bending test, the high transformability and effective crack deflection resulted in a better damage tolerance for this composite. In addition, an interesting phenomenon was that the Weibull plot of the three composites seemed to be composed of two regimes, i.e. a lower strength regime with a substantially higher modulus and a higher strength regime with a lower modulus (Fig. 8). In the strength regions ≤ 879 MPa for 12-20B, ≤ 857 MPa for 12-20P and ≤ 859 MPa for 12-20N, the composites showed steep Weibull strength distributions (m ≥ 80), whereas the apparent Weibull modulus for the high strength regions is substantially smaller. A similar result was reported for an alumina and strontium hexa-aluminate platelet toughened 2.5 mol% yttria stabilized zirconia composite, where the strength distribution consisted of two populations [74]. In these cases, the strength was restricted by two types of defects. The reinforcements by platelets seem to be able to eliminate the effect of large flaws and ensure a narrow strength distribution and a considerable minimum strength level.

At last, all three zirconia-alumina composites showed an excellent resistance to low temperature degradation. The *m*-ZrO_2 phase content remained the same as for the polished sintered composites after 150 hours of accelerated aging treatment.

4. Conclusions

Different alumina precursors had a considerable impact on the formation of fine grained elongated lanthanum hexa-aluminate precipitates and the concomitant mechanical performance of 12Ce-

TZP-based ATZ composites. Aluminium nitrate resulted in similar zirconia and alumina grain sizes as with α-alumina particles, but with smaller crack deflecting elongated lanthanum hexa-aluminate precipitates and a higher indentation fracture resistance. Boehmite as alumina precursor also gave rise to the small elongated $La_{0.9}Al_{11.7}O_{20.0}$ hexa-aluminate with a significant crack-deflecting capacity. Along with a higher transformability of the Ce-TZP phase, boehmite alumina precursor resulted in a ATZ composite combining the best indentation fracture resistance (9.7 MPa $m^{1/2}$), biaxial strength (σ_0=976 MPa) and reliability (m=20.7), as compared to the ATZ composites based on α-Al_2O_3 nanoparticles and aluminium nitrate.

Acknowledgements

Maoyin Li thanks the China Scholarship Council (CSC) for financial support (CSC No. 201806460096). This work was supported by the Research Fund of KU Leuven under project C24/17/084 and the Fund for Scientific Research Flanders (FWO-Vlaanderen) under grant G0B2618N. Fei Zhang thanks the Research Foundation - Flanders (FWO Vlaanderen) for her post-doctoral fellowship (12S8418N and 12S8421N). The authors gratefully acknowledge the Hercules Foundation for Project AKUL/1319 (CombiS(T)EM)).

Reference

[1] R.C. Garvie, R.H. Hannink, R.T. Pascoe, Ceramic steel?, Nature. 258 (1975) 703–704. https://doi.org/10.1038/258703a0.

[2] J. Chevalier, L. Gremillard, Ceramics for medical applications: A picture for the next 20 years, J. Eur. Ceram. Soc. 29 (2009) 1245–1255. https://doi.org/10.1016/j.jeurceramsoc.2008.08.025.

[3] F. Zhang, K. Vanmeensel, M. Batuk, J. Hadermann, M. Inokoshi, B. Van Meerbeek, I. Naert,

J. Vleugels, Highly-translucent, strong and aging-resistant 3Y-TZP ceramics for dental restoration by grain boundary segregation, Acta Biomater. 16 (2015) 215–222. https://doi.org/10.1016/j.actbio.2015.01.037.

[4] C. Piconi, W. Burger, H.G. Richter, A. Cittadini, G. Maccauro, V. Covacci, N. Bruzzese, G.A. Ricci, E. Marmo, Y-TZP ceramics for artificial joint replacements, Biomaterials. 19 (1998) 1489–1494. https://doi.org/10.1016/S0142-9612(98)00064-7.

[5] M. Turon-Vinas, F. Zhang, J. Vleugels, M. Anglada, Effect of calcia co-doping on ceria-stabilized zirconia, J. Eur. Ceram. Soc. 38 (2018) 2621–2631. https://doi.org/10.1016/j.jeurceramsoc.2017.12.053.

[6] L. Melk, M. Turon-Vinas, J.J. Roa, M.L. Antti, M. Anglada, The influence of unshielded small cracks in the fracture toughness of yttria and of ceria stabilised zirconia, J. Eur. Ceram. Soc. 36 (2016) 147–153. https://doi.org/10.1016/j.jeurceramsoc.2015.09.017.

[7] M. V. Swain, Impact of oral fluids on dental ceramics: What is the clinical relevance?, Dent. Mater. 30 (2014) 33–42. https://doi.org/10.1016/j.dental.2013.08.199.

[8] V. Turp, B. Tuncelli, D. Sen, G. Goller, Evaluation of hardness and fracture toughness, coupled with microstructural analysis, of zirconia ceramics stored in environments with different pH values, Dent. Mater. J. 31 (2012) 891–902. https://doi.org/10.4012/dmj.2012-005.

[9] J. Vleugels, C. Zhao, O. Van Der Biest, Toughness enhancement of Ce-TZP by annealing in argon, Scr. Mater. 50 (2004) 679–683. https://doi.org/10.1016/j.scriptamat.2003.11.017.

[10] P. Kohorst, L. Borchers, J. Strempel, M. Stiesch, T. Hassel, F.W. Bach, C. Hübsch, Low-temperature degradation of different zirconia ceramics for dental applications, Acta

Biomater. 8 (2012) 1213–1220. https://doi.org/10.1016/j.actbio.2011.11.016.

[11] J. Chevalier, L. Gremillard, A. V. Virkar, D.R. Clarke, The tetragonal-monoclinic transformation in zirconia: Lessons learned and future trends, J. Am. Ceram. Soc. 92 (2009) 1901–1920. https://doi.org/10.1111/j.1551-2916.2009.03278.x.

[12] H. Reveron, M. Fornabaio, P. Palmero, T. Fürderer, E. Adolfsson, V. Lughi, A. Bonifacio, V. Sergo, L. Montanaro, J. Chevalier, Towards long lasting zirconia-based composites for dental implants: Transformation induced plasticity and its consequence on ceramic reliability, Acta Biomater. 48 (2017) 423–432. https://doi.org/10.1016/j.actbio.2016.11.040.

[13] H. El Attaoui, M. Saâdaoui, J. Chevalier, G. Fantozzi, Static and cyclic crack propagation in Ce-TZP ceramics with different amounts of transformation toughening, J. Eur. Ceram. Soc. 27 (2007) 483–486. https://doi.org/10.1016/j.jeurceramsoc.2006.04.108.

[14] P. Palmero, M. Fornabaio, L. Montanaro, H. Reveron, C. Esnouf, J. Chevalier, Towards long lasting zirconia-based composites for dental implants: Part I: Innovative synthesis, microstructural characterization and invitro stability, Biomaterials. 50 (2015) 38–46. https://doi.org/10.1016/j.biomaterials.2015.01.018.

[15] S. Cailliet, M. Roumanie, R. Laucournet, G. Bernard-Granger, Sintering Ce-TZP/alumina composites using aluminum isopropoxide as a precursor, Ceram. Int. 45 (2019) 10530–10540. https://doi.org/10.1016/j.ceramint.2019.02.117.

[16] A.H. De Aza, J. Chevalier, G. Fantozzi, M. Schehl, R. Torrecillas, Crack growth resistance of alumina, zirconia and zirconia toughened alumina ceramics for joint prostheses, Biomaterials. 23 (2002) 937–945. https://doi.org/10.1016/S0142-9612(01)00206-X.

[17] R. Benzaid, J. Chevalier, M. Saâdaoui, G. Fantozzi, M. Nawa, L.A. Diaz, R. Torrecillas,

Fracture toughness, strength and slow crack growth in a ceria stabilized zirconia-alumina nanocomposite for medical applications, Biomaterials. 29 (2008) 3636–3641. https://doi.org/10.1016/j.biomaterials.2008.05.021.

[18] R. Marx, F. Jungwirth, P.O. Walter, Threshold intensity factors as lower boundaries for crack propagation in ceramics, Biomed. Eng. Online. 3 (2004) 1–9. https://doi.org/10.1186/1475-925X-3-41.

[19] H.I.L. R.A.Cutler, J.M.Lindemann, J.H.Ulvensøen, Damage resistant SrO-doped Ce-TZP/Al_2O_3 composites, Mater. Des. 15 (1994) 123–133. https://doi.org/10.1016/0261-3069(94)90111-2.

[20] M. Nawa, S. Nakamoto, K. Niihara, Tough and Strong Ce-TZP / Alumina Nanocomposites Doped with Titania, Ceram. Int. 24 (1998) 497–506. https://doi.org/10.1016/S0272-8842(97)00048-5.

[21] S. Huang, L. Li, J. Vleugels, P. Wang, O. Van Der Biest, Influence of Al_2O_3 Addition on the Microstructure and Mechanical Properties of Pressureless Sintered Ce-TZP, Mater. Sci. Forum. 492 (2005) 783–789. https://doi.org/10.4028/www.scientific.net/MSF.492-493.783.

[22] F. Zhang, K. Vanmeensel, M. Inokoshi, M. Batuk, J. Hadermann, B. Van Meerbeek, I. Naert, J. Vleugels, Critical influence of alumina content on the low temperature degradation of 2-3 mol% yttria-stabilized TZP for dental restorations, J. Eur. Ceram. Soc. 35 (2015) 741–750. https://doi.org/10.1016/j.jeurceramsoc.2014.09.018.

[23] V. Naglieri, P. Palmero, L. Montanaro, J. Chevalier, Elaboration of alumina-zirconia composites: Role of the zirconia content on the microstructure and mechanical properties, Materials (Basel). 6 (2013) 2090–2102. https://doi.org/10.3390/ma6052090.

[24] R.H.L. Garcia, V. Ussui, N.B. de Lima, E.N.S. Muccillo, D.R.R. Lazar, Physical properties of alumina/yttria-stabilized zirconia composites with improved microstructure, J. Alloys Compd. 486 (2009) 747–753. https://doi.org/10.1016/j.jallcom.2009.06.204.

[25] F. Kern, A comparison of microstructure and mechanical properties of 12Ce-TZP reinforced with alumina and in situ formed strontium- or lanthanum hexaaluminate precipitates, J. Eur. Ceram. Soc. 34 (2014) 413–423. https://doi.org/10.1016/j.jeurceramsoc.2013.08.037.

[26] Jing-Fong Tsai, U. Chon, N. Ramachandran, Dinesh K. Shetty, Transformation Plasticity and Toughening in CeO_2-Partially-Stabilized Zirconia–Alumina (Ce-TZP/Al_2O_3) Composites Doped with MnO, J. Am. Ceram. Soc. 75 (1992) 1229–1238. https://doi.org/10.1111/j.1151-2916.1992.tb05562.x.

[27] R.A. Cutler, R.J. Mayhew, K.M. Prettyman, A. V. Virkar, High-Toughness Ce-TZP/Al_2O_3 Ceramics with Improved Hardness and Strength, J. Am. Ceram. Soc. 74 (1991) 179–186. https://doi.org/10.1111/j.1151-2916.1991.tb07315.x.

[28] L. Gottwik, A. Wippermann, M. Kuntz, B. Denkena, Effect of strontium hexaaluminate addition on the damage-tolerance of yttria-stabilized zirconia, Ceram. Int. 43 (2017) 15891–15898. https://doi.org/10.1016/j.ceramint.2017.08.163.

[29] T. Fujii, H. Muragaki, H. Hatano, S.-I. Hirano, Microstructure Development and Mechanical Properties of Ce-TZP/La-β-Alumina Composites, MRS Online Proc. Libr. 274 (1992) 141–147. https://doi.org/10.1557/PROC-274-141.

[30] X. Huang, J. Cui, K. Guan, P. Rao, Influence of La_2O_3 addition on microstructure and mechanical properties of alumina-dispersed zirconia, (2021) 18–21.

[31] S.M. Lakiza, L.M. Lopato, Phase diagram of the Al_2O_3-ZrO_2 -La_2O_3 system, J. Eur. Ceram.

Soc. 25 (2005) 1373–1380. https://doi.org/10.1016/j.jeurceramsoc.2005.01.014.

[32] Mechanical property and microstructure of TZP and TZP/Al_2O_3 composites, 78 (1987) 123–135.

[33] M. Miura, H. Hongoh, T. Yogo, S. Hirano, T. Fujll, Formation of plate-like lanthanum-β-Aluminate crystal in Ce-TZP matrix, J. Mater. Sci. 29 (1994) 262–268. https://doi.org/10.1007/BF00356602.

[34] A. Liens, H. Reveron, T. Douillard, N. Blanchard, V. Lughi, V. Sergo, R. Laquai, B.R. Müller, G. Bruno, S. Schomer, T. Fürderer, E. Adolfsson, N. Courtois, M. Swain, J. Chevalier, Phase transformation induces plasticity with negligible damage in ceria-stabilized zirconia-based ceramics, Acta Mater. 183 (2020) 261–273. https://doi.org/10.1016/j.actamat.2019.10.046.

[35] C. Barrera-Solano, L. Esquivias, G.L. Messing, Effect of preparation conditions on phase formation, densification, and microstructure evolution in La-β-Al_2O_3/Al_2O_3 composites, J. Am. Ceram. Soc. 82 (1999) 1318–1324. https://doi.org/10.1111/j.1151-2916.1999.tb01914.x.

[36] R.C. Garvie, P.S. Nicholson, Phase Analysis in Zirconia Systems, J. Am. Ceram. Soc. 55 (1972) 303–305. https://doi.org/10.1111/j.1151-2916.1972.tb11290.x.

[37] H. Toraya, M. Yoshimura, S. Somiya, Calibration Curve for Quantitative Analysis of the Monoclinic-Tetragonal ZrO_2 System by X-Ray Diffraction, J. Am. Ceram. Soc. 67 (1984) C-119-C-121. https://doi.org/10.1111/j.1151-2916.1984.tb19715.x.

[38] W.M. Negahdari Z, Gerdes T, Microwave Enhanced Anisotropic Grain Growth in Lanthanum Hexa Aluminate-Alumina Composites, in: Mech. Prop. Perform. Eng. Ceram.

Compos. III, 2007: pp. 15–21.

[39] K. Niihara, R. Morena, O. Metals, Evaluation of K_{IC} of brittle solids by the indentation method with low crack-to-indent ratios, J. Mater. Sci. Lett. 1 (1982) 13–16. https://doi.org/10.1007/BF00724706.

[40] Gibson R F., Principles of composite material mechanics, CRC press, 2016.

[41] A. Yurdakul, Microstructural and mechanical characterization of ceria-stabilized tetragonal zirconia / alumina composites produced through a segregated-network approach for ceramic bushing applications, 57 (2021) 379–398. https://doi.org/https://doi.org/10.1007/s41779-020-00558-x.

[42] H.H. Kubota Y, Ashizuka M, Elastic modulus and fracture toughness of CeO_2-containing tetragonal zirconia polycrystals, J. Ceram. Soc. Japan. 102 (1994) 175–179. https://doi.org/https://doi.org/10.2109/jcersj.102.175.

[43] W. Pabst, G. Tichá, E.V.A. Gregorová, Effective elastic properties of alumina-zirconia composite ceramics-Part 3. Calculation of elastic moduli of polycrystalline alumina and zirconia from monocrystal data, Ceram. Silikaty. 48 (2004) 41–48.

[44] ISO 6872: 2015. Dentistry — Ceramic materials, ISO 6872. (2015).

[45] M. Xue, S. Liu, X. Wang, K. Jiang, High fracture toughness of 3Y-TZP ceramic over a wide sintering range, Mater. Chem. Phys. 244 (2020) 122693. https://doi.org/10.1016/j.matchemphys.2020.122693.

[46] Q. Jing, J. Bao, F. Ruan, X. Song, S. An, Y. Zhang, Z. Tian, M. Xie, J. Gao, The effect of YF3 on the mechanical properties and low-temperature degradation of 3Y-TZP ceramics, Ceram. Int. 45 (2019) 24212–24220. https://doi.org/10.1016/j.ceramint.2019.08.130.

[47] D. Fan, L.Q. Chen, S.P.P. Chen, Numerical simulation of Zener pinning with growing second-phase particles, J. Am. Ceram. Soc. 81 (1998) 526–532. https://doi.org/10.1111/j.1151-2916.1998.tb02370.x.

[48] M. Gasperin, M.C. Saine, A. Kahn, F. Laville, A.M. Lejus, I. Introduction, Influence of M^{2+} ions substitution on the structure of lanthanum hexaaluminates with magnetoplumbite structure, J. Solid State Chem. 54 (1984) 61–69. https://doi.org/10.1016/0022-4596(84)90131-2.

[49] B. Saruhan, H. Schneider, S. Komarneni, I.R. Abothu, Electrostatically deposited surface seeding and promotion of crystallization of sol-gel derived $LaAl_{11}O_{18}$ coating on oxide fibers, J. Eur. Ceram. Soc. 19 (1999) 2427–2435. https://doi.org/10.1016/s0955-2219(99)00115-6.

[50] Z. Negahdari, M. Willert-Porada, Tailoring the microstructure of reaction-sintered alumina/lanthanum hexaaluminate particulate composites, J. Eur. Ceram. Soc. 30 (2010) 1381–1389. https://doi.org/10.1016/j.jeurceramsoc.2009.10.010.

[51] J.J. Torrez-Herrera, E.G. Fuentes-Ordoñez, S.A. Korili, A. Gil, Evidence for the synthesis of La-hexaaluminate from aluminum-containing saline slag wastes: Correction of structural defects and phase purification at low temperature, Powder Technol. 377 (2021) 80–88. https://doi.org/10.1016/j.powtec.2020.08.087.

[52] J.G. Park, A.N. Cormack, Defect structures and nonstoichiometry in lanthanum hexa-aluminate, J. Eur. Ceram. Soc. 19 (1999) 2249–2256. https://doi.org/10.1016/s0955-2219(99)00123-5.

[53] R.R. Rao, L. Mariappan, Combustion synthesis and characterisation of lanthanum hexa-

aluminate, Adv. Appl. Ceram. 104 (2005) 268–271. https://doi.org/10.1179/174367605X62427.

[54] A. Boumaza, L. Favaro, J. Lédion, G. Sattonnay, J.B. Brubach, P. Berthet, A.M. Huntz, P. Roy, R. Tétot, Transition alumina phases induced by heat treatment of boehmite: An X-ray diffraction and infrared spectroscopy study, J. Solid State Chem. 182 (2009) 1171–1176. https://doi.org/10.1016/j.jssc.2009.02.006.

[55] J.A. Jiménez, I. Padilla, A. Lõpez-Delgado, L. Fillali, S. Lõpez-Andrés, Characterization of the aluminas formed during the thermal decomposition of boehmite by the rietveld refinement method, Int. J. Appl. Ceram. Technol. 12 (2015) E178–E186. https://doi.org/10.1111/ijac.12283.

[56] X. Du, Y. Wang, X. Su, J. Li, Influences of pH value on the microstructure and phase transformation of aluminum hydroxide, Powder Technol. 192 (2009) 40–46. https://doi.org/10.1016/j.powtec.2008.11.008.

[57] P. Melnikov, V.A. Nascimento, I. V. Arkhangelsky, L.Z. Zanoni Consolo, Thermal decomposition mechanism of aluminum nitrate octahydrate and characterization of intermediate products by the technique of computerized modeling, J. Therm. Anal. Calorim. 111 (2013) 543–548. https://doi.org/10.1007/s10973-012-2566-1.

[58] R. Gadow, M. Lischka, Lanthanum hexaaluminate — novel thermal barrier coatings for gas turbine applications — materials and process development, Surf. Coatings Technol. 151 (2002) 392–399. https://doi.org/10.1016/S0257-8972(01)01642-5.

[59] M.S. Khan, M.S. Islam, D.R. Bates, Cation doping and oxygen diffusion in zirconia: A combined atomistic simulation and molecular dynamics study, J. Mater. Chem. 8 (1998)

2299–2307. https://doi.org/10.1039/a803917h.

[60] F. Zhang, M. Batuk, J. Hadermann, G. Manfredi, A. Mariën, K. Vanmeensel, M. Inokoshi, B. Van Meerbeek, I. Naert, J. Vleugels, Effect of cation dopant radius on the hydrothermal stability of tetragonal zirconia: Grain boundary segregation and oxygen vacancy annihilation, Acta Mater. 106 (2016) 48–58. https://doi.org/10.1016/j.actamat.2015.12.051.

[61] F. Zhang, J. Chevalier, C. Olagnon, M. Batuk, J. Hadermann, B. Van Meerbeek, J. Vleugels, Grain-Boundary Engineering for Aging and Slow-Crack-Growth Resistant Zirconia, J. Dent. Res. 96 (2017) 774–779. https://doi.org/10.1177/0022034517698661.

[62] D. Tovar-Vargas, M. Turon-Vinas, M. Anglada, E. Jimenez-Pique, Enhancement of mechanical properties of ceria-calcia stabilized zirconia by alumina reinforcement, J. Eur. Ceram. Soc. 40 (2020) 3714–3722. https://doi.org/10.1016/j.jeurceramsoc.2020.02.002.

[63] F. Zhang, K. Vanmeensel, M. Inokoshi, M. Batuk, J. Hadermann, B. Van Meerbeek, I. Naert, J. Vleugels, 3Y-TZP ceramics with improved hydrothermal degradation resistance and fracture toughness, J. Eur. Ceram. Soc. 34 (2014) 2453–2463. https://doi.org/10.1016/j.jeurceramsoc.2014.02.026.

[64] M.K. Cinibulk, R.S. Hay, Textured magnetoplumbite fiber-matrix interphase derived from sol-gel fiber coatings, J. Am. Ceram. Soc. 79 (1996) 1233–1246. https://doi.org/10.1111/j.1151-2916.1996.tb08578.x.

[65] P.E.D. Morgan, D.B. Marshall, Functional interfaces for oxide/oxide composites, Mater. Sci. Eng. A. 162 (1993) 15–25. https://doi.org/10.1016/0921-5093(90)90026-Y.

[66] P.L. Swanson, C.J. Fairbanks, B.R. Lawn, Y.W. MAI, B.J. Hockey, Crack-Interface Grain Bridging as a Fracture Resistance I, Mechanism in Ceramics: I, Experimental Study on

Alumina, J. Am. Ceram. Soc. 70 (1987) 279–289. https://doi.org/10.1111/j.1151-2916.1987.tb04982.x.

[67] Y.W. MAI, B.R. Lawn, Crack-Interface Grain Bridging as a Fracture Resistance Mechanism in Ceramics: II, Theoretical Fracture Mechanics Model, J. Am. Ceram. Soc. 70 (1987) 289–294. https://doi.org/10.1111/j.1151-2916.1987.tb04983.x.

[68] D.B. Anstis, G. R., Chantikul, P., Lawn, B. R., & Marshall, A Critical Evaluation of Indentation Techniques for Measuring Fracture Toughness: I, Direct Crack Measurements, J. Am. Ceram. Soc. 64 (1981) 533–538.

[69] E. Apel, C. Ritzberger, N. Courtois, H. Reveron, J. Chevalier, M. Schweiger, F. Rothbrust, V.M. Rheinberger, W. Höland, Introduction to a tough, strong and stable Ce-TZP/$MgAl_2O_4$ composite for biomedical applications, J. Eur. Ceram. Soc. 32 (2012) 2697–2703. https://doi.org/10.1016/j.jeurceramsoc.2012.02.002.

[70] E.T.P. Bergamo, K.B. Cardoso, L.F.O. Lino, T.M.B. Campos, K.N. Monteiro, P.F. Cesar, L.A. Genova, G.P. Thim, P.G. Coelho, E.A. Bonfante, Alumina-toughened zirconia for dental applications: Physicochemical, mechanical, optical, and residual stress characterization after artificial aging, J. Biomed. Mater. Res. B Appl. Biomater. B Appl. Biomater. 109 (2020) 1135–1144. https://doi.org/10.1002/jbm.b.34776.

[71] M. Sakai, R.C. Bradt, Fracture toughness testing of brittle materials, Int. Mater. Rev. 38 (1993) 53–78. https://doi.org/10.1179/imr.1993.38.2.53.

[72] C. Oblak, P. Jevnikar, N. Funduk, L. Marion, The effect of surface grinding and sandblasting on flexural strength and reliability of Y-TZP zirconia ceramic, 15 (1999) 426–433.

[73] J. Chevalier, A. Liens, P. Reynaud, T. Douillard, M. Swain, N. Courtois, H. Reveron, F. Zhang, L. Preiss, V. Sergo, V. Lughi, Forty years after the promise of « ceramic steel ?»: Zirconia-based composites with a metal-like mechanical behavior, (2020) 1482–1513. https://doi.org/10.1111/jace.16903.

[74] F. Kern, R. Gadow, Influence of in-situ platelet reinforcement on the properties of injection moulded alumina-toughened zirconia, J. Ceram. Sci. Technol. 2 (2011) 47–54. https://doi.org/10.4416/JCST2010-00019.

[75] M.F. Kanninen, C.A. Popelar, H. Saunders, Advanced fracture mechanics, J. Vib. Acoust. Stress. Reliab. Des. 110 (1988) 419–420.

Figures

Fig. 1. XRD patterns of studied 12Ce-TZP based zirconia-alumina composites processed from α-alumina particles (12-20P), boehmite (12-20B) and aluminium nitrate (12-20N).

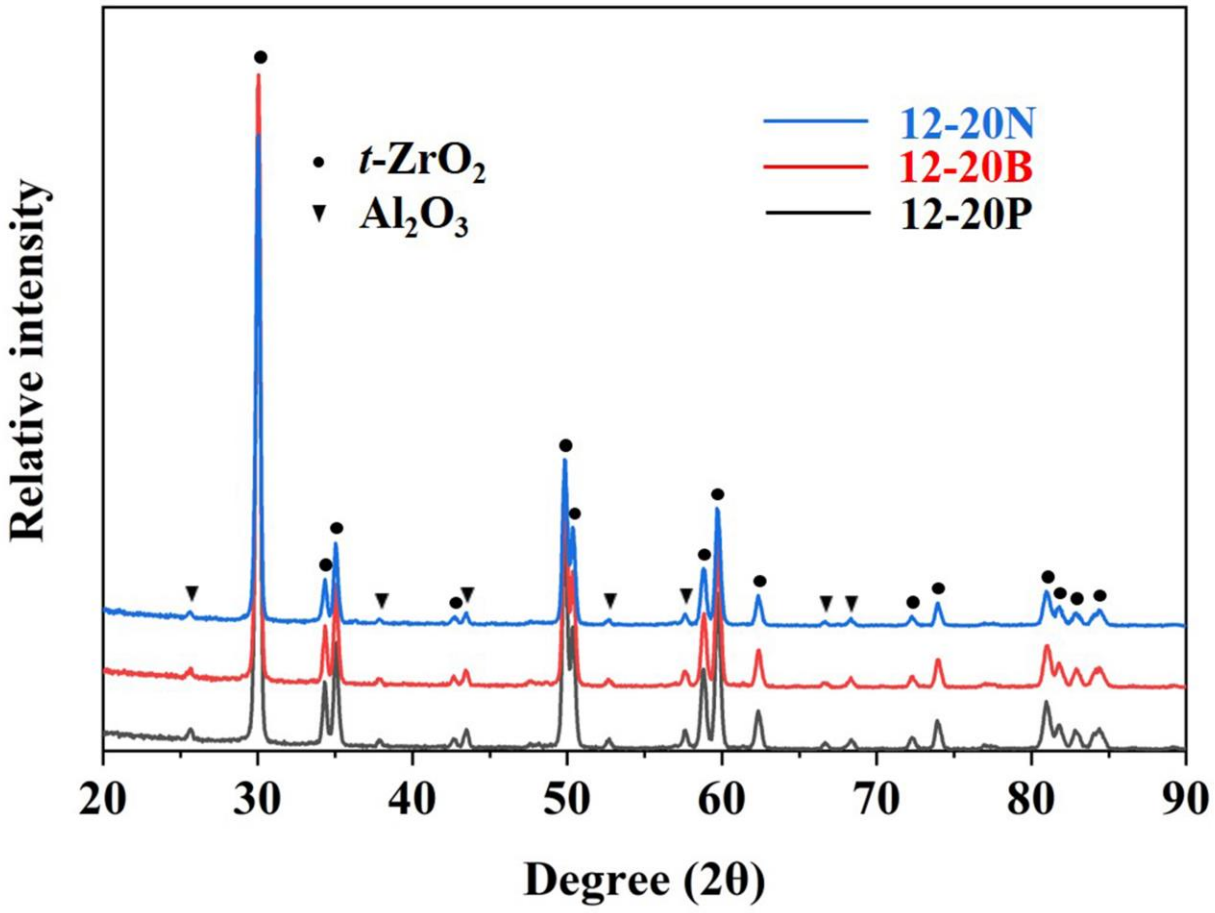

Fig. 2. SEM micrographs of (a, d) 12-20P; (b, e)12-20B; (c, f)12-20N.

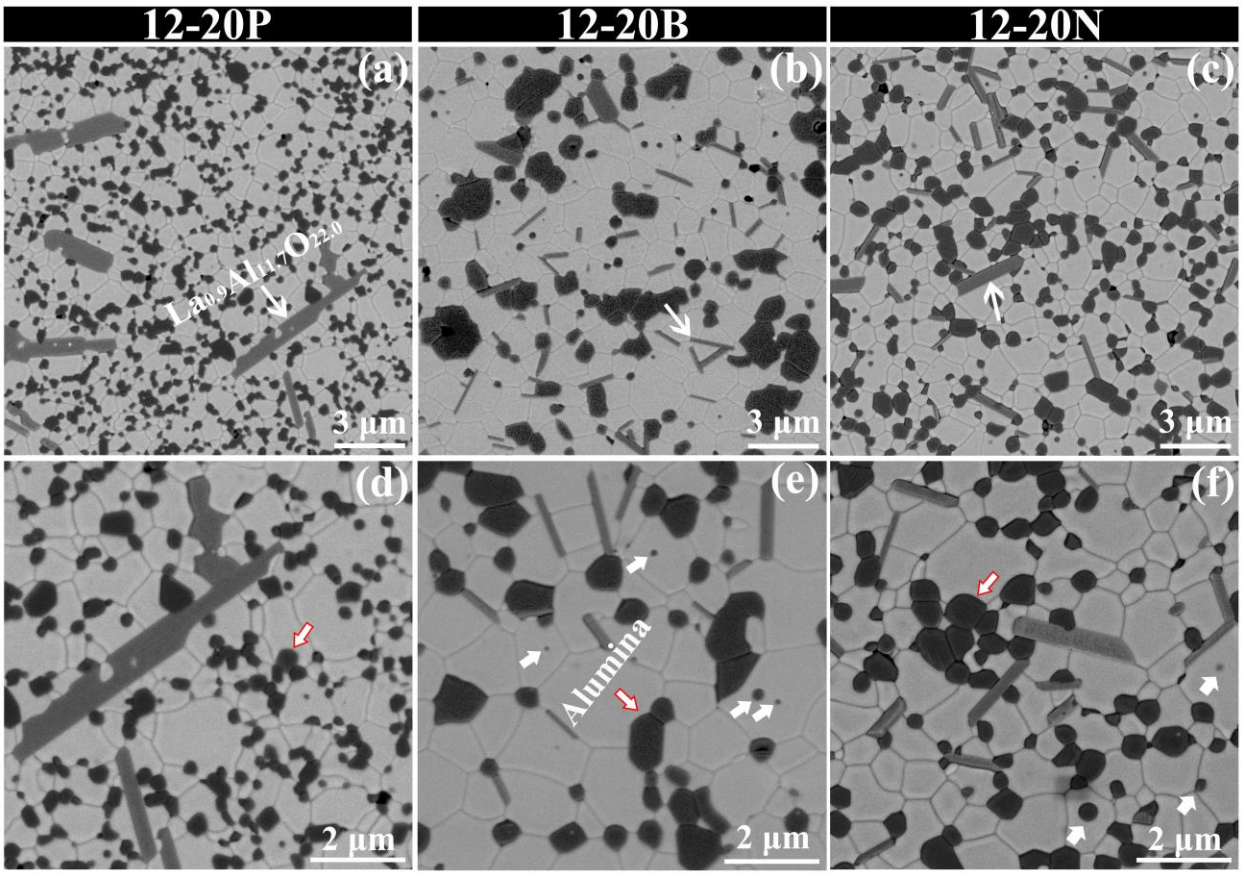

Fig. 3. Zirconia and alumina grain size and length of lanthanum hexa-aluminate ($La_{0.9}Al_{11.7}O_{20.0}$) distributions in (a, d and g) 12-20P, (b, e and h) 12-20B and (c, f and i) 12-20N.

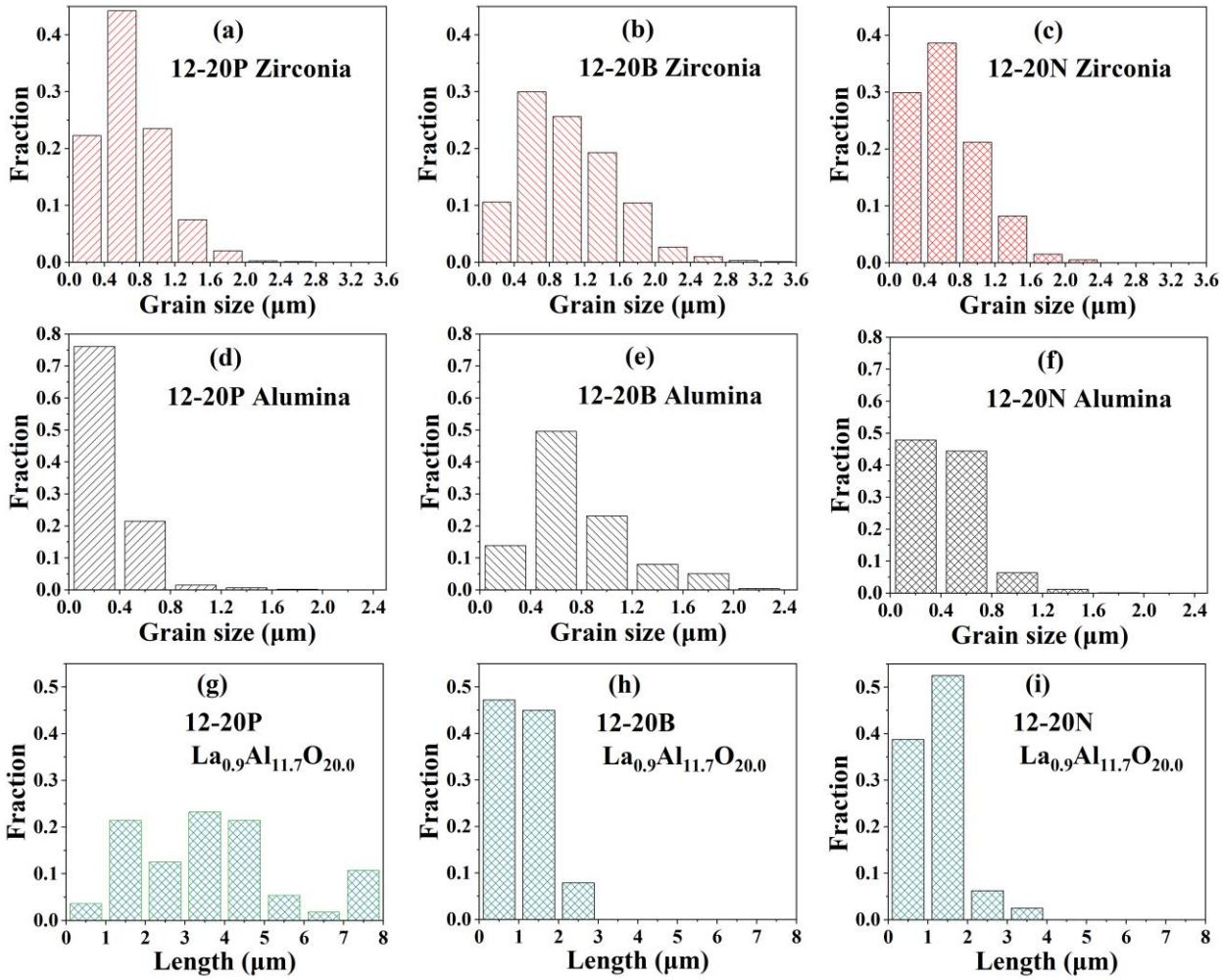

Fig. 4. (a) HAADF STEM Overview image of 12-20B; (b) HAADF STEM image of elongated $La_{0.9}Al_{11.7}O_{20.0}$ grain and indexed SAED at (c) $[2\bar{1}\bar{1}0]$ and at (d) $[01\bar{1}0]$ zone axes. (e) STEM/EDS maps of the same area in (a) with the elongated $La_{0.9}Al_{11.7}O_{20.0}$ grain in (b) marked.

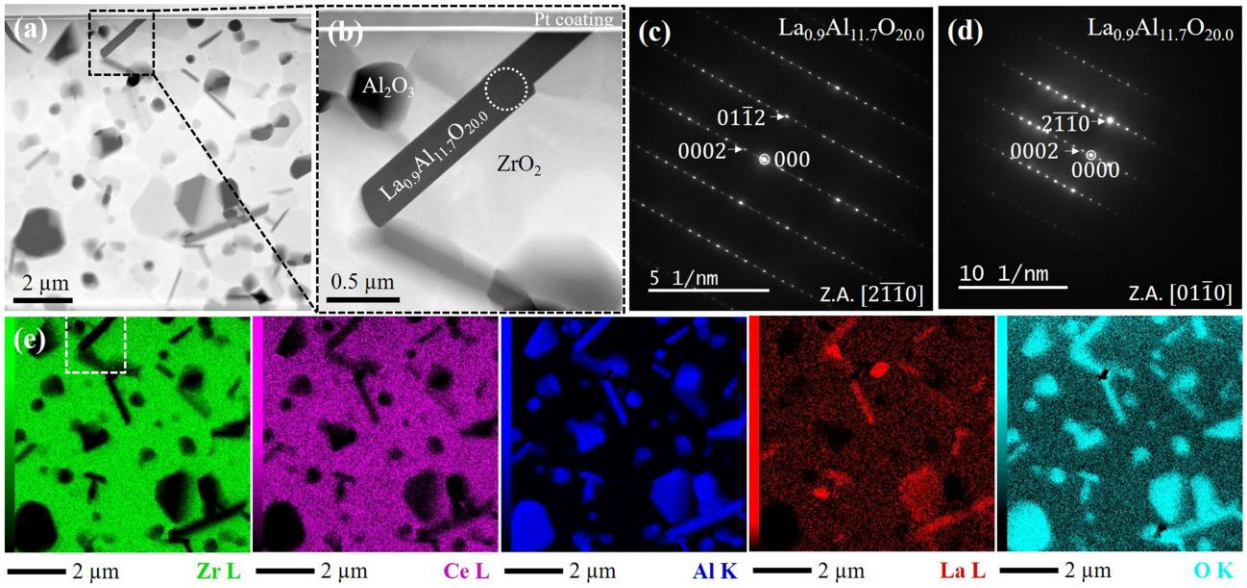

Fig. 5 STEM/EDS analysis: (a) Ce and La content variation across a ZrO_2-ZrO_2 grain boundary and (b) line scan across an elongated lanthanum hexa-aluminate ($La_{0.9}Al_{11.7}O_{20.0}$)-$ZrO_2$ grain boundary.

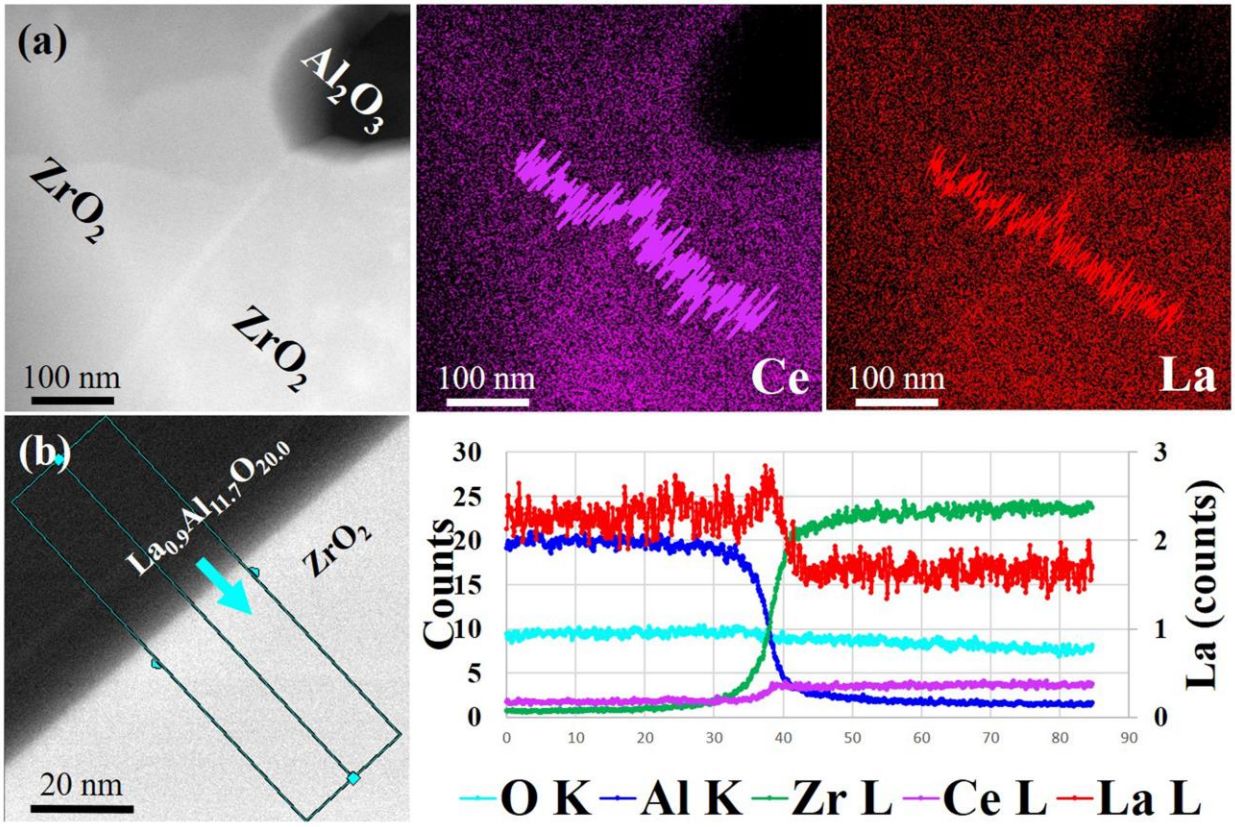

Fig. 6. Comparison of crack propagation paths in boehmite and alumina powder based composites (red arrow indicates the crack propagation direction). (a) Crack tip, (b) and (c) alumina and elongated grains enhanced crack deflection, (d) overall crack on 12-20B surface; (e), (f) and (g) crack on 12-20B surface.

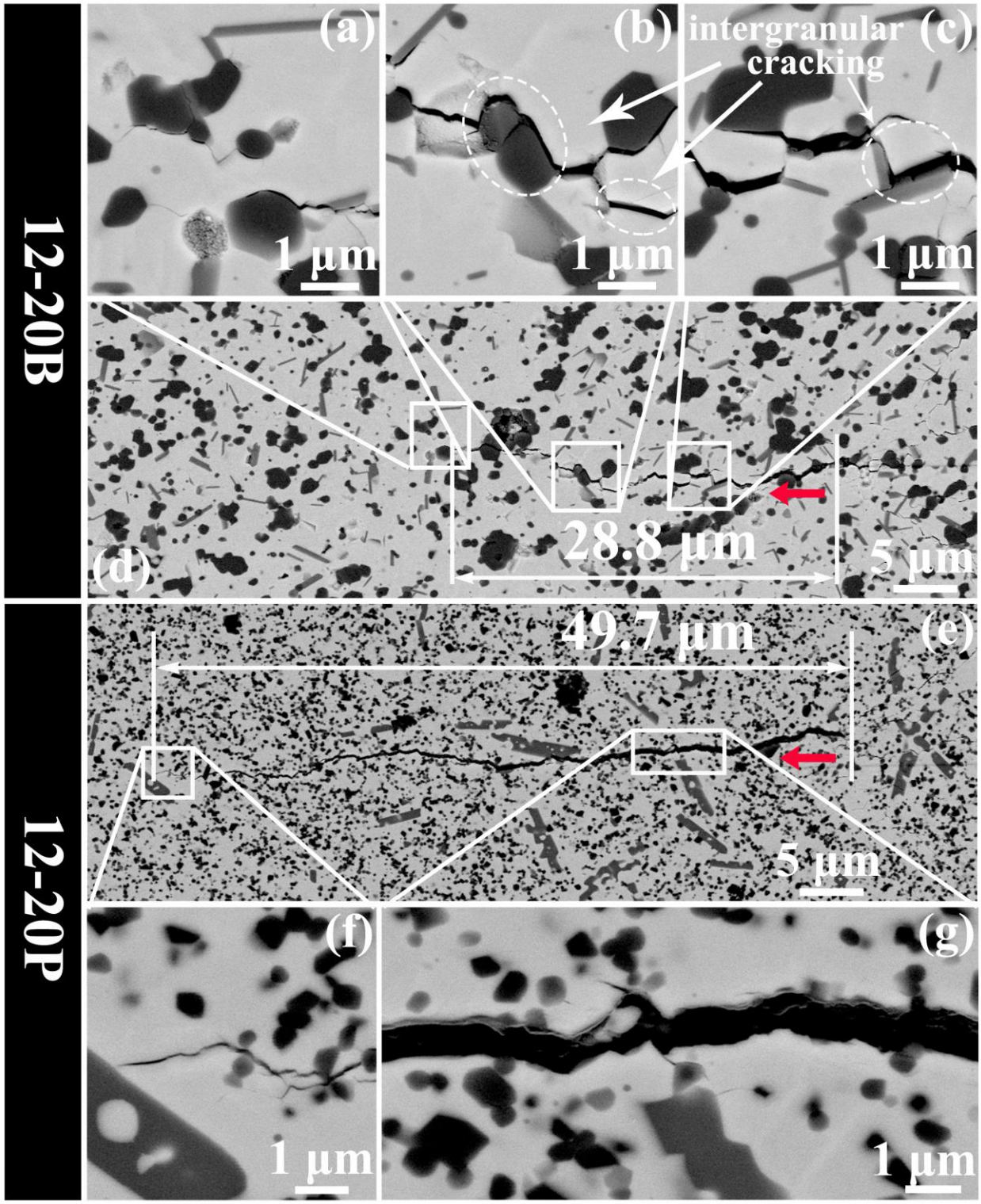

Fig. 7. Weibull plot of the biaxial flexural strength of 12-20P, 12-20B and 12-20N.

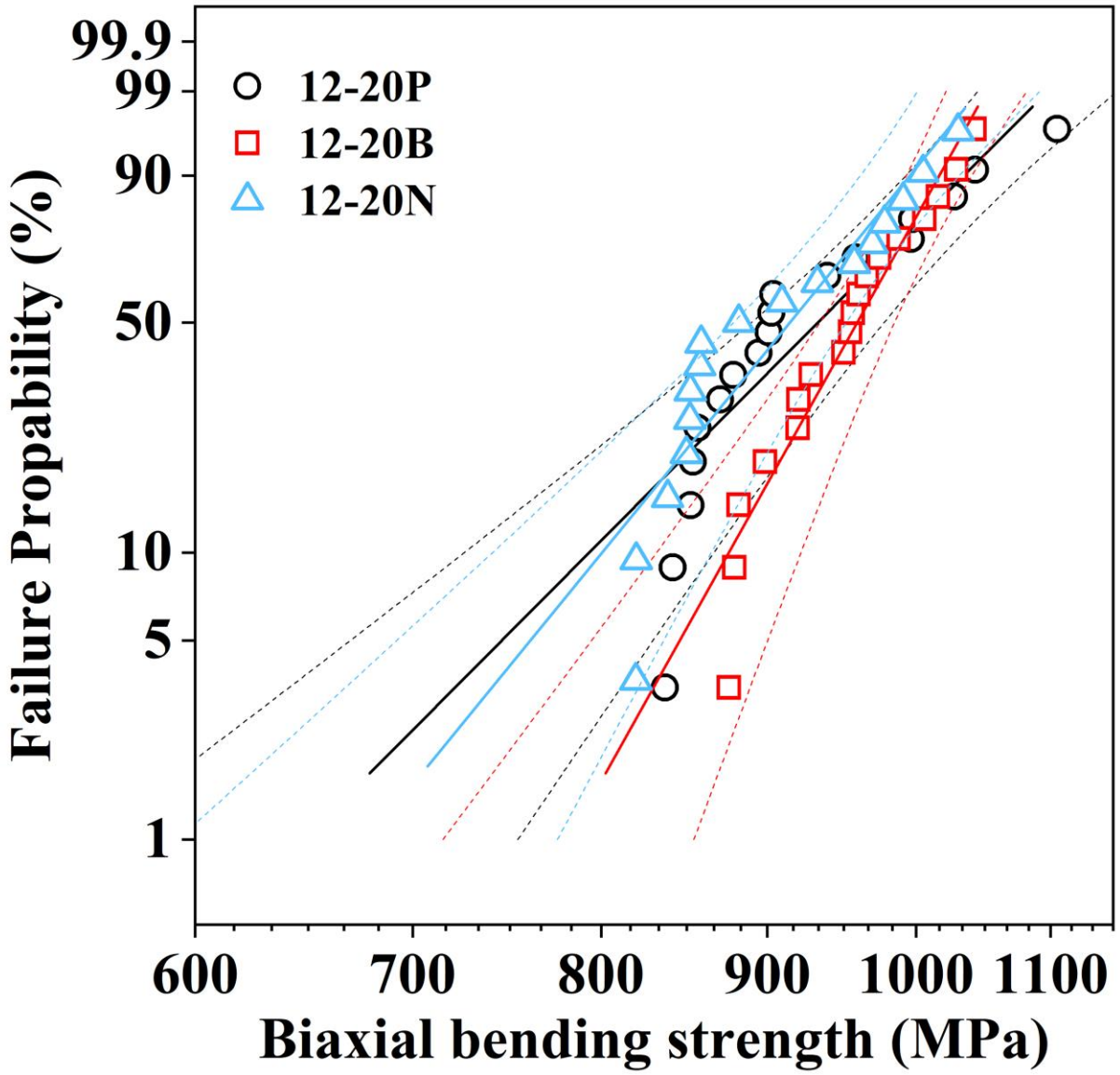

Fig. 8. Two regimes Weibull plot of the biaxial flexural strength of 12-20P, 12-20B and 12-20N, distinguishing a lower strength regime with a substantially higher modulus and a higher strength regime with a lower modulus.

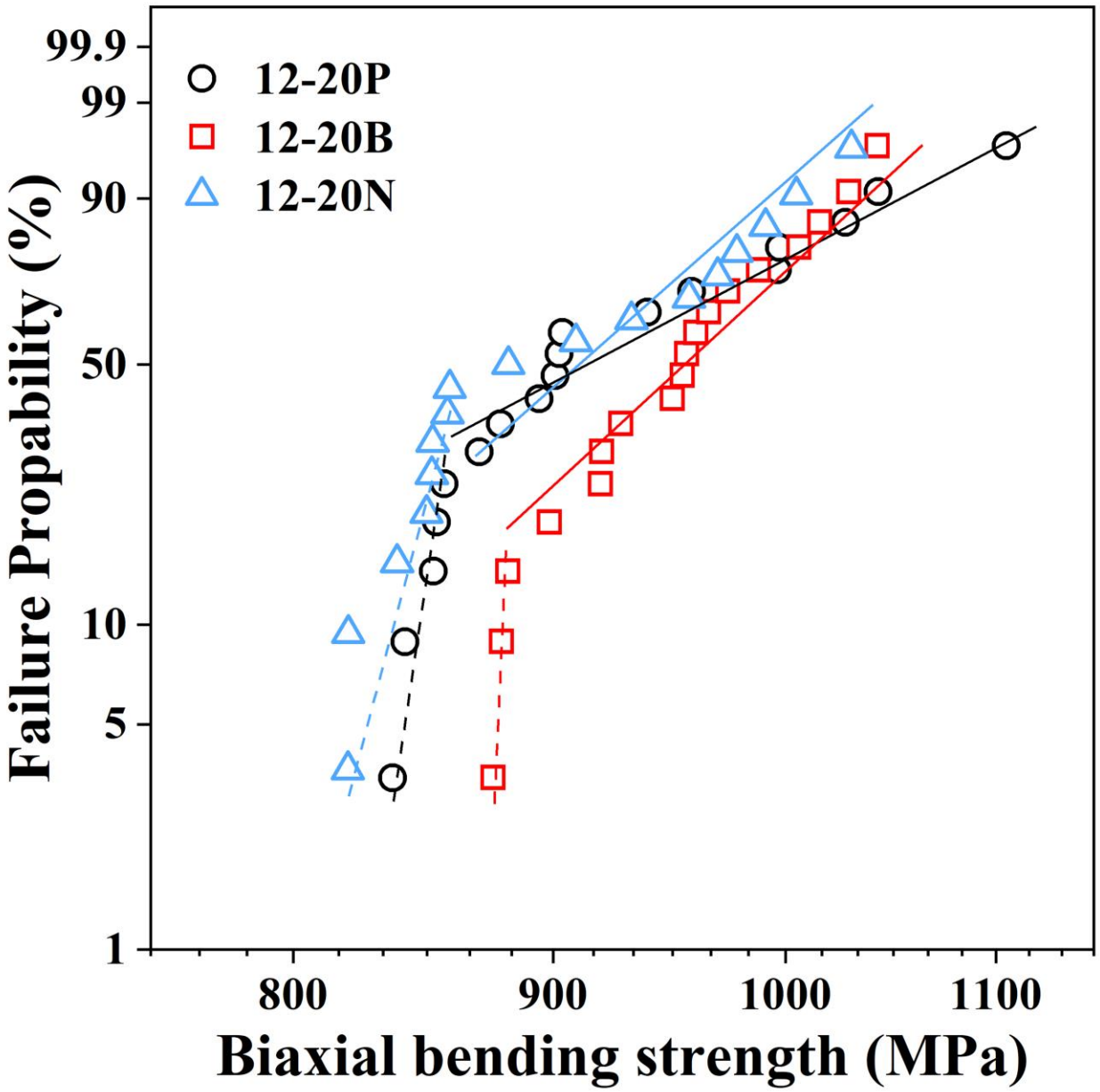

Tables

Table 1 Phase composition of the studied 12Ce-TZP based ATZ composites, as obtained by Rietveld refinement analyses

Ceramic	*c*-ZrO_2, vol%	*m*-ZrO_2, vol%	*t*-ZrO_2 Tetragonality	Al_2O_3, vol%
12-20B	1.60	2.16	1.01971	28.13
12-20P	1.31	2.34	1.01989	28.52
12-20N	1.79	2.43	1.01977	26.28

Table 2 Density of the investigated ATZ ceramics and the grain size of different phases.

sample	Density (g/cm^3)	Relative density (%)	Zirconia grain size (nm)	Alumina grain size (nm)	$La_{0.9}Al_{11.7}O_{20.0}$	
					length (μm)	aspect ratio
12-20P	5.59	99.3	705 [374]	335 [193]	3.5	4.4
12-20B	5.63	99.9	1018 [520]	759 [395]	1.1	5.6
12-20N	5.61	99.6	662 [387]	453 [232]	1.3	5.6

Table 3 Mechanical properties and *t*-ZrO_2 phase transformability of 12-20B, 12-20P, 12-20N ATZ ceramics (σ_0: Weibull characteristic strength, m: Weibull modulus of strength data)

sample	Hardness (GPa)	Toughness ($MPa \cdot m^{1/2}$)	*t*-ZrO_2 transformability (vol%)	σ_0 (MPa)	m
12-20P	11.5 [0.1]	6.7 [0.3]	17	962	11.6
12-20B	10.6 [0.1]	9.7 [0.5]	36	976	20.7
12-20N	11.1 [0.1]	8.0 [0.5]	16	939	14.1